J Mater Sci (2007) 42:6153–6160
DOI 10.1007/s10853-006-1134-0

Laser multi-layer cladding of $Zr_{65}Al_{7.5}Ni_{10}Cu_{17.5}$ amorphous alloy on magnesium substrates

Tai Man Yue · Yun P. Su

Received: 29 July 2006 / Accepted: 13 October 2006 / Published online: 17 April 2007

Abstract A coating about 3-mm thick of the amorphous alloy, $Zr_{65}Al_{7.5}Ni_{10}Cu_{17.5}$ was fabricated on magnesium substrates using the technique of laser multi-layer cladding protected under an atmosphere of argon gas. The coating exhibited a graded microstructure, which could be generally categorized into three classes: an amorphous phase, an amorphous–nanocrystalline composite, and one which is predominantly crystalline. Formation of the latter two was due to the reheating effect of the laser cladding process. With regard to properties, the microhardness and the wear resistance of the composite material were both higher than that of the monolithic amorphous material; both materials showed excellent corrosion resistance in a 3.5% NaCl solution.

Introduction

Magnesium alloys offer great potential for applications where weight-saving is of prime consideration. Unfortunately, magnesium alloys have the undesirable properties of poor corrosion resistance and wear resistance that have hindered the widespread application of these materials. The extreme position of magnesium in the electrochemical series coupled with the fact that magnesium cannot form self-healing passivating surface films in corrosive environments makes it vulnerable to galvanic attack. Over the years, intensive research efforts have been devoted to overcoming these shortcomings. Currently, the most commonly used surface modification technologies applied to magnesium alloys include electrochemical plating, conversion coating, anodizing, gas-phase deposition processes and organic coating [1]. However, to date, it is still difficult to find a single coating technology capable of providing adequate protection from corrosion and abrasion for magnesium alloys in harsh service environments. For instance, anodizing coatings have excellent wear and abrasion resistance, but the coatings are not suitable for load-bearing applications [2].

One surface engineering technique, namely laser cladding, has attracted much attraction in recent years. Its main advantage over other techniques is its ability to form a variety of relatively thick protective coatings and it is a cleaner process than many of the chemicals-based wet processes. Previous studies have shown that laser surface treatment can improve the corrosion resistance of magnesium alloys [3–6]. Now, by using laser cladding of metallic amorphous coatings, further improvements in corrosion and wear resistance are expected. Up to now, only a few studies on the laser cladding of amorphous alloys can be found in the literature. Audebert et al. [7] and Wang et al. [8] have successfully produced partial Zr-based amorphous phase coatings on aluminium and titanium substrates, respectively. Other amorphous alloys, which are based on the system of Ni–Cr–Al with a high critical cooling rate, have also been used for laser cladding of amorphous layers on aluminium alloys [9]. However, similar studies of laser cladding of amorphous coatings on magnesium alloys can rarely be found in the literature. This is probably because the relatively low melting and vaporization temperatures as well as the ease of oxidation of magnesium alloys makes the cladding process difficult to control. But, these problems could be overcome by proper design of the experiment [10, 11].

T. M. Yue (✉) · Y. P. Su
The Advanced Manufacturing Technology Research Centre, Department of Industrial and Systems Engineering, The Hong Kong Polytechnic University, Hung Hom, Hong Kong
e-mail: mftmyue@inet.polyu.edu.hk

Since the first synthesis of a metallic amorphous phase in 1960, great efforts have been made to develop glassy metallic alloys, which by nature have excellent corrosion resistance [12]. With the recently developed amorphous materials that have a large glass-forming ability [13, 14], it is now possible to produce metallic amorphous coatings using the laser-cladding technique. With regard to mechanical properties of amorphous materials, it was found that bulk fully amorphous materials have the problem of low ductility, which has limited the application of amorphous materials. In the course of the development of amorphous materials, amorphous matrix composites (AMCs) have received much attention in recent years. Although the corrosion resistance of AMCs may not be as good as the monolithic alloys, they possess higher ductility and better mechanical properties [15]. Among the AMCs, homogeneous nanocrystalline–amorphous composites exhibit high hardness and high tensile strength and outstanding wear resistance with improved ductility [16, 17]. Such composites are normally formed by reheating to elevated temperatures or mechanical deformation of amorphous alloys. As reheating of amorphous materials to elevated temperatures is a common route to the synthesis of these composites, it is possible to fabricate such composite coatings using multiple-layer laser cladding. In using laser cladding to form amorphous-based coatings on metal substrates, it was commonly found that, depending on the processing parameters, an amorphous phase predominant coating or a crystalline phase predominant coating can be formed. Apparently, the constituting phases of the coating will markedly affect its corrosion and wear properties. Scully et al. [18] has reported that the localized corrosion properties of two Al-rich glass alloys formed by the technique of melt spinning, are very different in the amorphous and crystalline states. It is envisaged that by forming a suitable nanocrystalline–amorphous composite on magnesium substrates, a coating with reasonably good corrosion resistance and excellent wear resistance can be produced. With this background in mind, this study aims to establish the relationship between the microstructure and the corrosion resistance as well as the wear resistance of $Zr_{65}Al_{7.5}Ni_{10}Cu_{17.5}$ glass alloy laser cladded on a magnesium alloy.

Experimental approach

Laser cladding of $Zr_{65}Al_{7.5}Ni_{10}Cu_{17.5}$ amorphous alloy was conducted on a magnesium substrate, which has a purity of 99.9 wt% and a surface area of 30 mm × 30 mm. The elemental metal powders were premixed according to the nominal atomic percentage composition of $Zr_{65}Al_{7.5}Ni_{10}Cu_{17.5}$. The composition, size and purity of the constituting powders are listed in Table 1. The powders were mixed by a ball mill in an argon gas atmosphere. The laser cladding experiment was carried out using a laser rapid forming system consisting of a 5 kW continuous wave CO_2 laser, a four-axis numerical control working table and a powder feeder with a lateral nozzle. The experiment was conducted inside a glove box, where high-purity argon gas was continuously supplied at a flow rate of 25 L/min to prevent the melting pool from oxidation during processing. The working principle of the system has been described previously [19]. The laser beam was directed onto the substrate to create a molten pool into which the premixed powders were injected through the powder feed nozzle; the powder feed rate was 7.5 g/min. This was different from the precoat method that was commonly used for laser cladding of amorphous alloys. In the present work, the laser beam was focused to a spot size of 3 mm. The scanning rate was 5 mm/s and the laser power employed was 4.0 kW. On each substrate, a single track was produced, which consists four layers of deposition and the total thickness of the coating was about 3.0 mm.

Transmission electron microscopy (TEM) was used to examine the microstructure of the coatings. Specimen foils with a thickness of about 0.5 mm were taken parallel to the surface of the coating, from the top, middle and bottom locations. These specimens were labeled A, B and C, respectively. Furthermore, transverse cross-sections of the coating were also prepared. TEM specimens were obtained by electropolishing using a twin jet polisher. A Philips EM 420 transmission electron microscope was employed for the study. In addition to TEM, the microstructure was examined by a Leica Stereoscan 440 scanning electron microscope (SEM) with an energy dispersive X-ray spectroscopy (EDS) and a Philips Xpert XRD System with CuK_{α} radiation.

The microhardness of the coating was measured at various depths across the coating. The wear properties of the coating were investigated using a Sciland pin-on-disc

Table 1 Specification of the metal powders

Element	Zr	Al	Ni	Cu
Mixing ratio (at%)	65	7.5	10	17.5
Purity (mass %)	99.90	99.90	99.95	99.95
Size (mesh)	200–300	200–300	200–300	200–300

tribometer. The specimens for the wear test have a size of 10 mm × 10 mm. A normal load of 300 g was used; the test was conducted at room temperature. The rotational speed of the disc was 150 rpm and the total sliding time for the test was 1 h. In the corrosion tests, both the potentiodynamic polarization technique and electrochemical impedance spectroscopy (EIS) were employed to evaluate the corrosion behaviour of the coatings. The corrosion potential was measured with respect to a saturated calomel electrode (SCE); the test was performed in a 3.5 wt% NaCl solution which was prepared using analytical grade reagents. The initial pH value of the solution was 6.46, and after the test the value changed to 6.38. The initial temperature of the solution was 25 °C. Prior to the electrochemical test, the specimens were ground with 800 grit emery papers, and cleaned with deionized water and alcohol. Before each polarization scan was initiated, the specimen was allowed to stabilize in the electrolyte. For the EIS experiment, a sinusoidal voltage of 5 mV and a frequency range of 1×10^5 to 1×10^{-2} Hz were used and the test was conducted under the open-circuit potential condition.

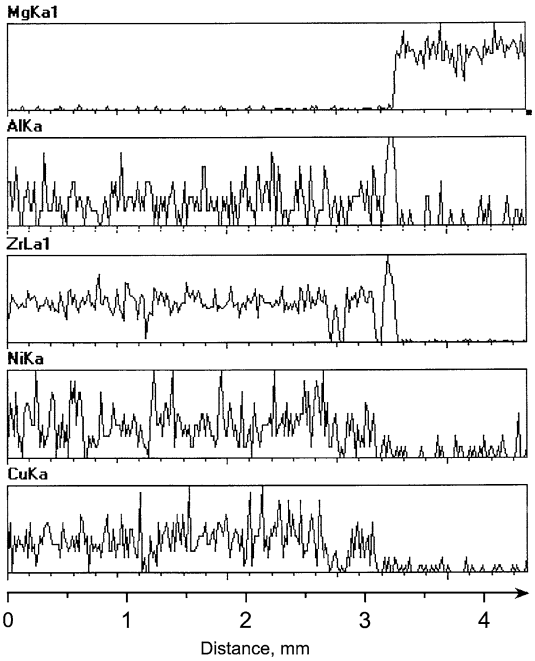

Fig. 2 Distribution of alloy elements across the substrate and the coating

Results and discussion

Microstructure

Figure 1 shows a low-magnification optical image of the cross-section of the coating, which has a thickness of about 3.0-mm thick. No cracks or voids are observed within the coating. Figure 2 shows the constitutional distribution of the alloy elements in the coating as well as the coating–substrate interface region. In general, the coating has a reasonably uniform distribution of alloy elements. Although, there is indication of a mixing zone of the cladding material and substrate material at the interface region (Fig. 2), a rather sharp substrate–coating interface was observed. An EDS line scan of the interface region (Fig. 3) showed that the extent of the mixing was only short range, only about 40 μm, and there was no evidence of a considerable amount of Mg having entered the coating. This is believed to be due to the limited solubility of Mg in Zr. The absence of such a dilution effect is important to guarantee the formation of the $Zr_{65}Al_{7.5}Ni_{10}Cu_{17.5}$ amorphous phase and to ensure good corrosion resistance for the coating.

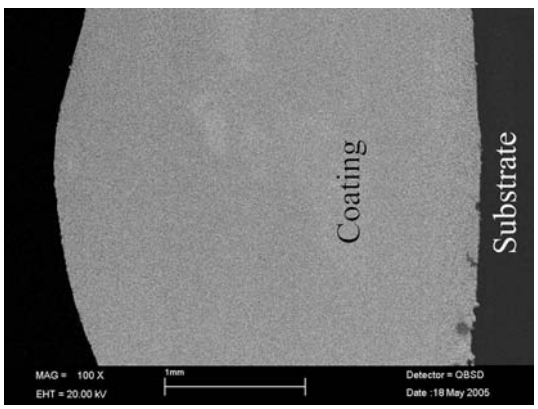

Fig. 1 SEM micrograph showing a transverse cross-section of the coating

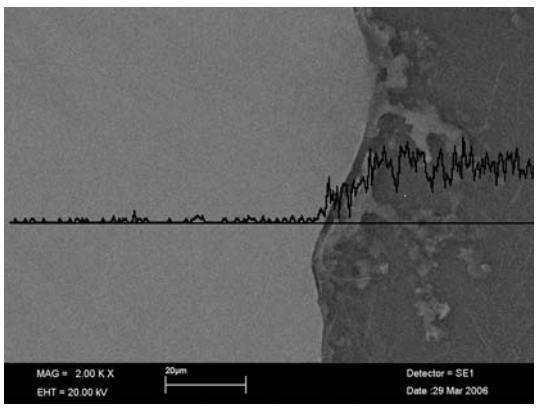

Fig. 3 SEM micrograph of the coating–substrate interface and an EDS line scan of magnesium across the interface

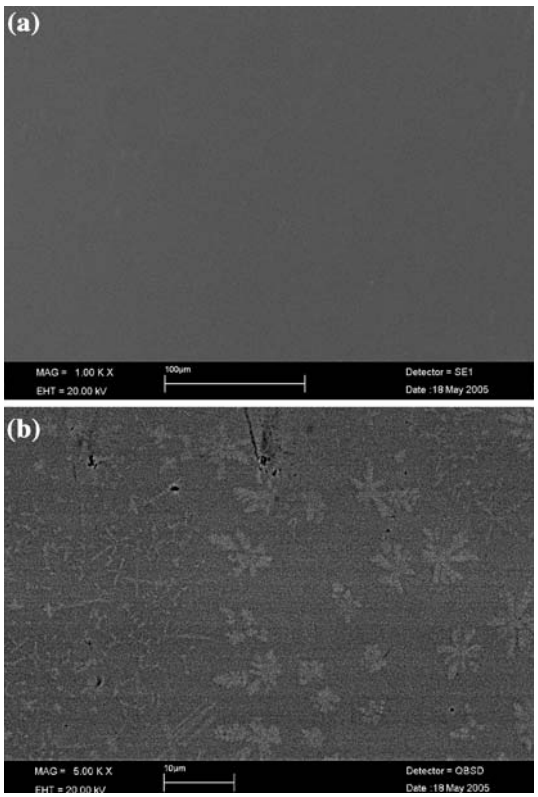

Fig. 4 Transverse cross-sections of the coating (**a**) near the surface, and (**b**) towards the bottom

Figure 4(a, b) shows the transverse cross-section SEM images of the coating near the surface and toward the bottom position, respectively: a kind of featureless structure was observed near the surface of the coating, while dendritic structures with sizes ranging from 1 to 10 μm were found embedded in the matrix toward the bottom section of the coating. An EDS analysis showed that the composition of the featureless structure was close to the desired composition of the amorphous alloy. The microstructure of the coating was further studied using TEM. Figure 5(a–c) shows the TEM images obtained for specimens A, B and C, respectively. The broad halo ring in Fig. 5a is a selected-area electron diffraction (SAED) pattern taken of the microstructure of Fig. 5a, which indicates that this region consists primarily of an amorphous phase. For specimen B, a dark field image shows that at a position in the middle of the coating, the microstructure comprises some fine precipitates with a diameter less than 30 nm (Fig. 5b). A SAED pattern of this microstructure shows both continuous diffraction rings and halo rings, suggesting that nanocrystals have developed in a matrix of amorphous phase. While in specimen C (Fig. 5c), i.e., at the bottom position of the coating, some relatively coarse crystalline particles are found in a mixed crystalline–amorphous matrix. The SAED pattern (bottom insert in Fig. 5c) of one of these particles (P) clearly shows that it is a crystalline phase, while a SAED pattern of the matrix (M) indicates that it comprises crystalline and amorphous phases (top insert in Fig. 5c).

Figure 6 shows the XRD patterns of specimens A, B and C. The pattern of specimen A reveals that the microstructure is in an amorphous state, and the XRD results agreed with the findings of Inoue et al. [20] for the $Zr_{65}Al_{7.5}Ni_{10}Cu_{17.5}$ amorphous phase. The XRD pattern of specimen B indicates that the microstructure is a mixture of crystalline and amorphous phases. This result agreed with

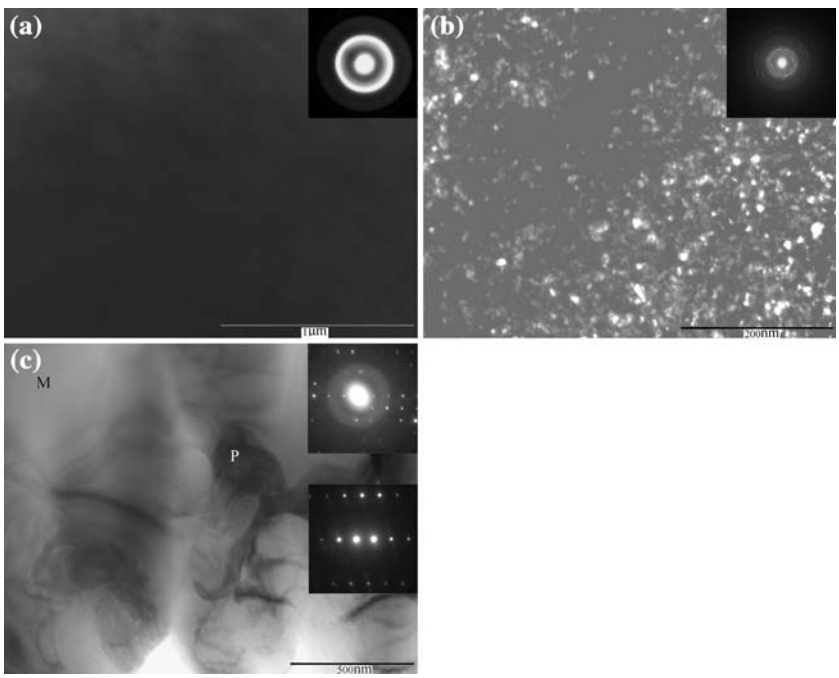

Fig. 5 TEM images and SAED patterns of (**a**) specimen A, (**b**) specimen B, and (**c**) specimen C

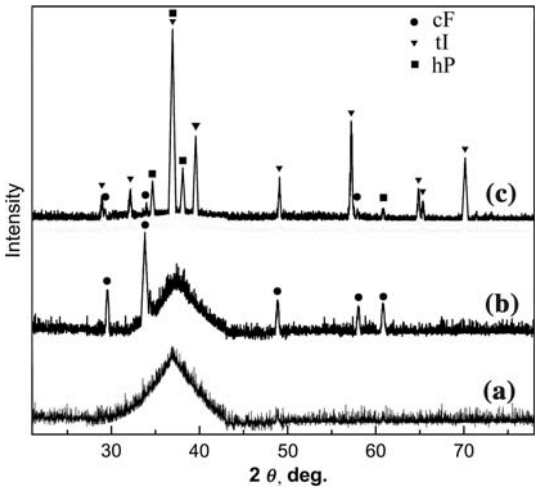

Fig. 6 X-ray diffraction patterns of specimens A, B and C

the TEM image (Fig. 5b) which indicated formation in the middle section of the coating, of a composite consisting of an amorphous phase and a nano-scale face-centered cubic phase (0.5272 nm). For specimen C, the XRD pattern shows that in the microstructure, there are two crystalline phases and an amorphous phase. The two crystalline phases were identified as hexagonal hP-$Zr_{65.4}Al_{11.7}Ni_{11.6}Cu_{11.3}$ phase (0.8209, 0.3329 nm) and body-centered tetragonal tI-$Zr_{67.0}Al_{1.7}Ni_{8.4}Cu_{22.9}$ phase (0.3212, 1.1146 nm). These two phases have been reported to be the products of crystallization in cast $Zr_{65}Al_{7.5}Ni_{10}Cu_{17.5}$ amorphous alloy [21]. The SAED pattern shown in Fig. 5c (bottom insert) corresponds to the tI phase. The dendritic structures observed in Fig. 4b are believed to be of this phase. From the collective results of TEM, SAED and XRD, it can be concluded that the coating roughly consists of three sections with different types of microstructure; this is supported by the microhardness measurements presented in a later section. Up to about one-third of the thickness of the coating measuring from the top, the microstructure is composed primarily of the amorphous phase $Zr_{65}Al_{7.5}Ni_{10}Cu_{17.5}$; in the middle of the coating, a composite of amorphous–nanocrystalline structure was formed. In fact, a similar microstructure was observed in a Zr-based amorphous alloy after annealing at 645 K [22]. Also, nanocrystals were produced in Zr-based alloys by reheating of the amorphous phase with proper processing parameters [23]. Towards the bottom of the coating, a crystalline dominant structure with a trace of amorphous phase was evident.

The formation of the amorphous–nanocrystalline composite is considered to be due to the reheating effect of the laser multiple-layer cladding process. In the cladding experiment, four layers were deposited on the substrate. The top surface layer will not experience a reheating effect since it is the last layer to be deposited. It is known that the critical cooling rate for the formation of the amorphous phase was about 1.5 K/s for the present Zr–Al–Ni–Cu alloy [20], and in laser cladding, the cooling rate is normally in the order of 10^3 K/s or even higher [24]. Therefore, the solidified microstructure of the top layer is expected to be in an amorphous state. For the rest of the layers, the original solidified structure should also be amorphous. However, due to the subsequent heating effect from the cladding of the overlaying layers, nucleation of crystalline phases would be induced. Previous studies have shown that the size of the crystalline phase, which nucleates in an amorphous phase increased with decreasing reheating/cooling rate and increasing reheating time [25]. It is apparent that such a condition was experienced by the layers when traveling towards the substrate. Indeed, the size of the crystalline phases was found to have increased towards the bottom of the coating (Fig. 4b).

Wear and corrosion properties

Figure 7 shows the microhardness of the coating at various depths from the surface: the hardness rose sharply in the middle of the coating and reached a peak value of about 700 HV at a distance 1.8 mm from the surface. This peak value was much higher than that of the amorphous phase located at the upper portion of the coating. As the microstructure of the middle section of the coating is composed of amorphous and nanocrystalline phases, the increase in microhardness is attributed to the reinforcement of the nanocrystalline particles. Towards the bottom of the coating, the microhardness decreased. This is believed to be due to the coarsening of the crystal phases. An abrupt drop in hardness was obtained at the coating–substrate interface; this is due to a rather distinct interface with only a narrow mixing zone of the cladding and substrate materials.

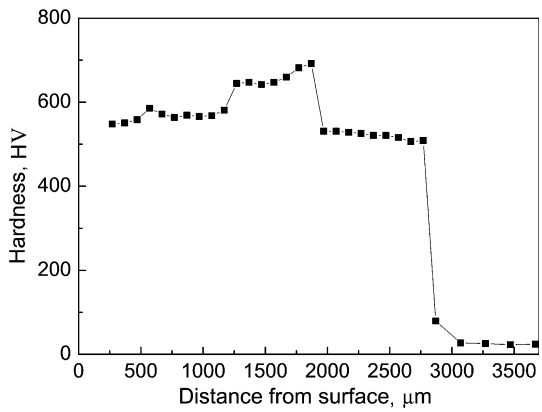

Fig. 7 Microhardness values measured across the coating

From the results of the wear test, the average volumetric loss of the substrate and those specimens extracted from the top and middle portions of the coating were obtained and are presented in Table 2. These specimens represent the microstructure of the substrate Mg, a full amorphous alloy, and an amorphous–nanocrystalline composite, respectively. In terms of volumetric loss, both the full amorphous alloy and the amorphous–nanocrystalline composite exhibited a much higher wear resistance than the substrate. The wear resistance of the amorphous–nanocrystalline composite was some 16 times higher than that of the substrate and was slightly higher than that of the full amorphous alloy. This showed that the nanocrystals improved the wear resistance of the amorphous alloy. Figure 8 shows the change of coefficient of friction of the amorphous–nanocrystalline composite specimen with time. After a sliding distance of 100 m, the coefficient of friction of the specimen has only reached a figure of 0.3, which is significantly lower than the figure of 0.52 obtained for the as-cast $Zr_{65}Al_{7.5}Ni_{10}Cu_{17.5}$ amorphous alloy [8]. Furthermore, with increasing testing time, the coefficient only increased slightly. The increase was probably mainly due to some relatively hard nanocrystals which were detached from the coating.

To compare the corrosion properties of the various microstructures, potentiodynamic anodic polarization curves were obtained for the amorphous layer, the amorphous–nanocrystalline composite and the substrate. These specimens were extracted from different positions of the laser-clad sample. Typical potentiodynamic polarization curves of these specimens are shown in Fig. 9. Although, the region of passivity was doubled for the amorphous phase, the open-circuit corrosion current density (i_{corr}) and the corrosion potential (E_{corr}) were nearly the same for the amorphous and the amorphous–nanocrystalline materials. The i_{corr} of the these two specimens was significantly lower than that obtained for the magnesium-based substrates that were coated with Al–12Si alloy [26] or stainless steel [27] by laser cladding when tested under a similar corrosion condition. This indicates that both the amorphous layer and the amorphous–nanocrystalline composite have superior corrosion resistance to the untreated material and many other laser-clad Mg-based materials. The fact that the

Table 2 Average volumetric loss measured after a wear testing time of 1 h

Specimen	Average volumetric loss [range of five measurements] ($\times 10^{-3}$ mm^3)	
Amorphous	6.1	[4.4–8.4]
Amorphous–nanocrystalline composite	5.3	[3.7–6.9]
Substrate	83.4	[63.4–122.5]

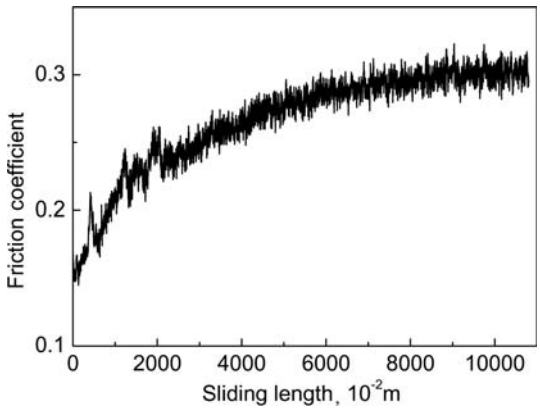

Fig. 8 The coefficient of friction measured for the amorphous–nanocrystalline composite

passive region of the amorphous–nanocrystalline composite was smaller than that of the amorphous phase, and the pitting potential of the former was some 150 mV lower than that of the latter, indicates that the presence of nanocrystals in the matrix of amorphous phase had resulted in a decrease of corrosion resistance. This could be mainly due to compositional inhomogeneity caused by the crystallization of the nanocrystalline phases in the amorphous matrix as these phases are different in composition to the glassy phase. Consequently, pitting sites could be developed at interface regions between the nanocrystals and the amorphous matrix.

The potentiodynamic polarization test primarily measures the corrosion activities of the vulnerable corrosion sites on the surface of a test specimen. To evaluate the corrosion response of the surface layer as a whole, the EIS experiment was conducted and the results were displayed as Nyquist plots. The plots for the amorphous layer and the amorphous–nanocrystalline composite are shown in Fig. 10(a) and (b), respectively. The plots of both

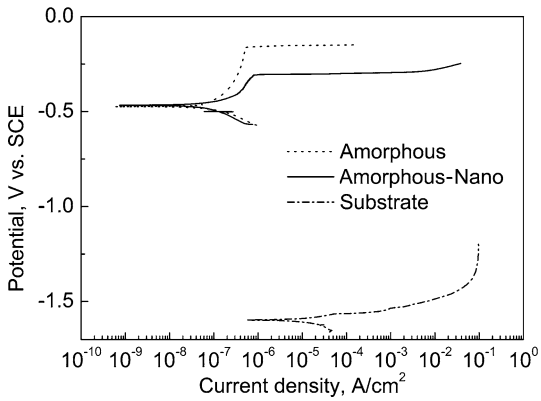

Fig. 9 Potentiodynamic anodic polarization curves of the untreated, the amorphous and the amorphous–nanocrystalline composite specimens

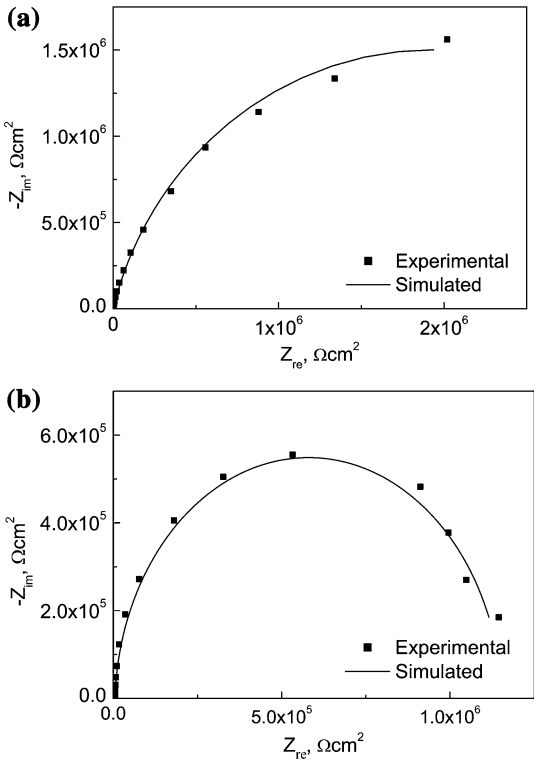

Fig. 10 Nyquist plots for the (**a**) amorphous structure, and (**b**) amorphous–nanocrystalline composite, tested in a 3.5-wt% NaCl solution under the open-circuit potential condition

specimens consist of only one capacitive loop, indicating that the process of electron-transfer was the prime electrochemical activity. This implies that both the amorphous layer and the amorphous–nanocrystalline composite have similar electrochemical corrosion behaviour under the open-circuit potential condition. The equivalent circuit shown in Fig. 11 is employed to interpret the EIS spectra. The equivalent circuit component values have been calculated and are presented in Table 3. The polarization resistance of the surface layers of both specimens was very high, indicating that both the amorphous and amorphous–nanocrystalline composite were in a passivation state and this agrees with the results of the potentiodynamic polarization test. Moreover, the EIS measurements (Fig. 10)

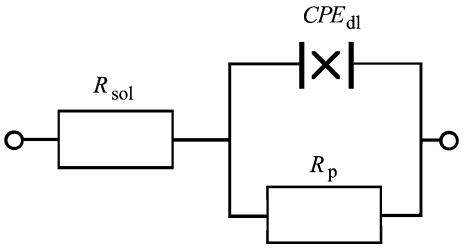

Fig. 11 Equivalent circuit for fitting the one capacitive loop impedance plots, as shown in Fig. 11. R_{sol} represents solution resistance; CPE_{dl} represents the capacitance of the surface layer; and R_p represents polarization resistance of surface layer

Table 3 Calculated values of the equivalent circuit components of the plots shown in Fig. 11

Specimens	C_{dl} μFcm^{-2}	R_p Ω
Amorphous	2.65	3.86×10^6
Amorphous–nanocrystalline composite	2.20	1.17×10^6

indicated that an effect of the film-diffusion was insignificant and that the electrode reaction was controlled only by charge transfer. This indicates that a stable and tight passive oxide layer of Zr is most likely developed at the surface of the coating, despite the presence of nanocrystals in a matrix of amorphous phase.

Conclusions

The $Zr_{65}Al_{7.5}Ni_{10}Cu_{17.5}$ alloy can be laser cladded on magnesium substrates with a good metallurgical bond without formation of sizeable porosity or cracks at the coating–substrate interface. In addition, a rather sharp coating–substrate interface was formed with no evidence of any significant diffusion of magnesium into the coating. With regard to the microstructure, under the condition of this study, the alloy solidified broadly into three types of structures: towards the top of the coating, an amorphous phase was produced; in the middle portion, an amorphous–nanocrystalline composite was formed; while towards the bottom section, it was primarily in crystalline form. Those crystalline phases were resulted from the crystallization of the amorphous layer induced by the reheating during cladding of the subsequent layers.

The microhardness of the amorphous–nanocrystalline composite was found to be higher than that of the monolithic amorphous layer. The former has a higher wear resistance than the latter. Regarding corrosion properties, the corrosion resistance of magnesium was significantly increased by laser cladding of the amorphous layer at the surface, when tested in a 3.5% NaCl solution. Both the amorphous layer and the amorphous–nanocrystalline composite showed excellent polarization resistance with the former better than the latter.

Acknowledgements The work described in this paper was fully supported by a grant from the Research Grants Council of the Hong Kong Special Administrative Region, China (Project No. PolyU 5315/04E). The authors also thank the Hong Kong Polytechnic University and Northwetern Polytechnical University for providing the research facilities.

References

1. Gray JE, Luan B (2002) J Alloys Compd 336:88

2. Nakatsugawa I (June 1996) In Proceedings of IMA 53, magnesium—a material advancing to the 21st century, Yamaguchi, Japan, International Magnesium Association, USA, p 24
3. Shibaev VV, Gulayeva TV, Shimchenyuk LA (1991) Protect Metals 26:606
4. Galun R, Weisheit A, Mordike BL (1996) J Laser Appl 8:299
5. Wang AA, Sircar S, Mazumder J (1993) J Mater Sci 28:5113, doi: 10/1007/BF00570050
6. Guo LF, Yue TM, Man HC (2005) J Mater Sci 40(13):3531, doi: 10.1007/10853-005-2888-5
7. Audebert F, Colaco R, Vilar R, Sirkin H (2003) Scripta Mater 48:281
8. Wang YF, Li G, Wang CS, Xia YL, Sandip B, Dong C (2004) Surface Coat Technol 176:284
9. Liang GY, Wong TT, Su JY, Woo CH (2000) J Mater Sci Let 19:1193
10. Subramanian R, Sircar S, Mazumder J (1991) J Mater Sci 26:951, doi:10.1007/BF00576771
11. Yue TM, Su YP, Yang HO (2007) Mater Lett 61(1):209
12. Hashimoto K, Kumagai N, Yoshioka H, Kim JH, Akiyama E, Habazaki H, Mrowec S, Kawashima A, Asami K (1993) Corros Sci 35(1–4):363
13. Inoue A, Zhang T, Masumoto T (1993) J Non-Cryst Solids 473:156
14. Inoue A (2000) Acta Mater 48:279
15. Xu YK, Xu J (2003) Scripta Mater 49:843
16. Sun WS, Quan MX (1996) Mater Lett 27:101
17. Greer AL (2001) Mater Sci Eng A 304–306:68
18. Sweitzer JE, Shiflet GJ, Scully JR (2003) Electrochim Acta 48:1223
19. Lin X, Yue TM, Yang HO, Huang WD (2005) Mater Sci Eng A 391:325
20. Inoue A, Zhang T, Nishiyama N, Ohba K, Masumoto T (1993) Mater Trans JIM 34:1234
21. Shek CH, Wang YM, Dong C (2000) Mater Sci Eng A 291:78
22. Kim SJ, Kim YH, Yang YS (2001) Mater Sci Eng A 304–306:767
23. Xing LQ, Eckert J, Loïser W, Schultz L, Herlach DM (1999) Philos Mag A 79:1095
24. Jendrzejewski R, Śliwiński G, Krawczuk M, Ostachowicz W (2004) Comput Struct 82:653
25. Kelton KF (1993) J Non-Cryst Solids 163:283
26. Yue TM, Wang AH, Man HC (1999) Scripta Mater 40:303
27. Yue TM, Hu QW, Mei Z, Man HC (2001) Mater Lett 47:165